ACS APPLIED MATERIALS & INTERFACES

Research Article

Cite This: ACS Appl. Mater. Interfaces 2019, 11, 45796−45804

www.acsami.org

Semi-Transparent Perovskite Solar Cells with ITO Directly Sputtered on Spiro-OMeTAD for Tandem Applications

Alexander J. Bett,*[,†] Kristina M. Winkler,[†] Martin Bivour,[†] Ludmila Cojocaru,[‡] Özde Ş. Kabakli,[†] Patricia S. C. Schulze,[†] Gerald Siefer,[†] Leonard Tutsch,[†] Martin Hermle,[†] Stefan W. Glunz,[†,‡] and Jan Christoph Goldschmidt[†]

[†]Fraunhofer Institute for Solar Energy Systems ISE, Heidenhofstrasse 2, 79110 Freiburg, Germany

[‡]Laboratory for Photovoltaic Energy Conversion, Department for Sustainable Systems Engineering (INATECH), University of Freiburg, Emmy-Noether-Strasse 2, 79110 Freiburg, Germany

Supporting Information

ABSTRACT: Perovskite silicon tandem solar cells have the potential to overcome the efficiency limit of single-junction solar cells. For both monolithic and mechanically stacked tandem devices, a semi-transparent perovskite top solar cell, including a transparent contact, is required. Usually, this contact consists of a metal oxide buffer layer and a sputtered transparent conductive oxide. In this work, semi-transparent perovskite solar cells in the regular n−i−p structure are presented with tin-doped indium oxide (ITO) directly sputtered on the hole conducting material Spiro-OMeTAD. ITO process parameters such as sputter power, temperature, and pressure in the chamber are systematically varied. While a low temperature of 50 °C is crucial for good device performance, a low sputter power has only a slight effect, and an increased chamber pressure has no influence on device performance. For the 5 × 5 mm^2 perovskite cell with a planar front side, a 105 nm thick ITO layer with a sheet resistance of 44 Ω sq^{-1} allowing for the omission of grid fingers and a MgF_2 antireflection coating are used to improve transmission into the solar cells. The best device achieved an efficiency of 14.8%, which would result in 24.2% in a four-terminal tandem configuration.

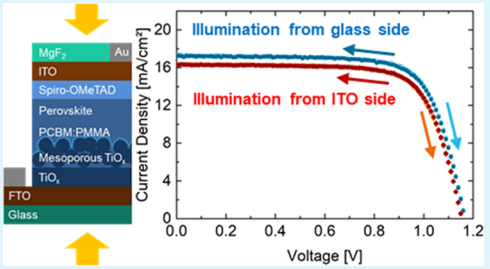

KEYWORDS: *perovskite solar cells, perovskite silicon tandem solar cells, tin-doped indium oxide, sputter process, process optimization*

1. INTRODUCTION

Since their emergence in photovoltaics, perovskite solar cells have achieved an unprecedentedly fast development. As a direct semiconductor, perovskites show a high absorption coefficient and a sharp absorption edge.[1] They can be fabricated at potentially low processing costs using solution or vacuum-based techniques.[2−5] The efficiency has increased up to 25.2% in only a few years.[6] A specific feature of perovskites is the tunable band gap over a wide range by compositional engineering.[7−9] Therefore, perovskite solar cells are promising candidates as a top cell in perovskite silicon tandem solar cells.

Silicon solar cells have already achieved efficiencies over 26%.[10] However, silicon single-junctionsolar cells are limited to an efficiency of 29.4%.[11] This limit can be overcome by tandem solar cells using a top cell with a larger band gap than silicon reducing thermalization losses. The optimal top cell band gap for a silicon bottom solar cell is ∼1.7 eV,[12] which can be achieved with a mixed-cation mixed-halide perovskite absorber.[7]

Generally, tandem devices can be realized by mechanically stacking (four-terminal configuration) or monolithically interconnecting (two-terminal configuration) the two subcells. With both configurations, remarkable efficiencies of over 25% could already be achieved.[13−17] Both configurations have their special advantages. In the case of mechanically stacked tandem solar cells, both cells can be optimized independently. No current matching is needed. However, a more complex module connection would be required than in the case of single-junction solar cells, and several laterally conductive layers are needed. In two-terminal devices, current matching is required. However, less laterally conductive layers are needed, and in consequence, lower parasitic absorption could be expected. Additionally, a standard module layout known from silicon technology can be applied.

In both cases, a semi-transparent top solar cell is required for transmitting the photons with energies lower than the perovskite band gap to the silicon solar cells underneath, i.e., the full area metal contact typically deposited as the last step in the production of single-junction perovskite solar cells needs to be replaced by a transparent conductive layer. This can be realized in different ways. Silver nanowires, graphene-based electrodes, and very thin metal layers have been proposed.[13,18−24] Problems of these methods are the complex

Received: September 23, 2019
Accepted: November 15, 2019
Published: November 15, 2019

fabrication method and stability issues for nanowires, a high sheet resistance for graphene layers with high transmission, and strong parasitic absorption in the case of thin metal layers.[25,26] The most common solution for the front side contact in semi-transparent perovskite solar cells or tandem solar cells is using a transparent conductive oxide (TCO), often tin-doped indium oxide (ITO) or indium-doped zinc oxide (IZO).[9,14−16,27−42] These layers are usually deposited by a sputter process. To avoid sputter damage of the layers underneath, buffer layers are typically deposited before sputtering the TCO. In the case of the regular n−i−p architecture, which allows for the highest perovskite single-junction solar cell efficiencies so far,[43−47] the most common buffer layer is evaporated molybdenum oxide (MoO_x).[28−32,34−40,42] Some groups also used solution-processed metal oxide nanoparticles.[9,27] Dewi et al. used a 1 nm thick silver buffer layer before sputtering ITO and achieved 17.7% efficiency.[41] Shen et al. achieved 18.1% efficiency for semi-transparent perovskite solar cells with MoO_x and IZO.[40] With a contact consisting of MoO_x and ITO, efficiencies of ∼17% were achieved.[30,42] The drawback is that an additional process step is required when using a buffer layer. Additionally, the use of MoO_x leads to enhanced parasitic absorption.[26,48,49] Therefore, it was proposed to replace MoO_x by tungsten oxide (WO_x).[48] Nevertheless, there was only little effort omitting the buffer layer and sputtering the TCO directly on the charge carrier selective contact. Werner et al. achieved 9.7% efficiency for semi-transparent perovskite solar cells with IZO directly sputtered on 2,2′,7,7′-tetrakis(*N*,*N*-di-*p*-methoxyphenylamine)-9,9-spirobifluorene (Spiro-OMeTAD), and Fu et al. achieved ∼10% with hydrogenated indium oxide (In_2O_3:H).[37,50] For further improvement, in both cases MoO_x was used. Jaysankar et al. used ITO directly sputtered on Spiro-OMeTAD in four-terminal perovskite silicon tandem modules and achieved 14.4% efficiency with the corresponding perovskite single-junction solar cells.[51] However, they did not go into detail about the sputter parameter optimization.

In this paper, we present semi-transparent perovskite solar cells in the regular n−i−p structure using a soft ITO process, which can be directly applied to Spiro-OMeTAD without the need for a buffer layer. Therefore, the sputtering process for the ITO has been adapted. Our semi-transparent cells reach efficiencies of up to 14.8% and good reproducibility. We use an electron contact passivation layer allowing for an open-circuit voltage (V_{OC}) over 1.1 V and a high band gap absorber suitable for perovskite silicon tandem devices. From transmittance measurements of the semi-transparent perovskite solar cells and the quantum efficiency of a high-efficiency silicon solar cell, we calculate the resulting J_{SC} of the silicon solar cell under our semi-transparent perovskite solar cell. We then measured the efficiency of the silicon solar cell with the reduced J_{SC}. The addition of the two measured efficiency results in an overall efficiency of 24.2% for the four-terminal tandem device.

2. RESULTS

2.1. Solar Cell Architectures. ITO sputter parameters (sputter power, temperature and pressure in the chamber) were systematically varied in several experiments. As in parallel work, other layers have also been optimized, not all experiments have been carried out with exactly the same solar cell structure, but results from other studies have been included. Altogether, three different generations of perovskite solar cells have been used for the ITO optimization (Figure 1).

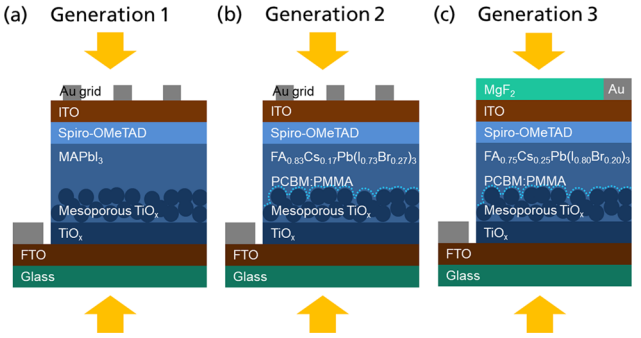

Figure 1. Schematic structures of the perovskite solar cells used in this work. (a) First generation of solar cells using $MAPbI_3$ as absorber material and a front side contact grid. (b) Second generation of solar cells using a mixed-cation mixed-halide absorber ($FA_{0.83}Cs_{0.17}Pb(I_{0.73}Br_{0.27})_3$) and a PCBM:PMMA passivation layer on the electron contact. (c) Third generation of solar cells with a slightly adapted absorber composition ($FA_{0.75}Cs_{0.25}Pb(I_{0.80}Br_{0.20})_3$), a MgF_2 antireflection coating, and no contact grid in the active cell area.

In all generations, semi-transparent perovskite solar cells were fabricated in the regular n−i−p architecture on fluorine-doped tin oxide (FTO)-coated glass substrates. Compact and mesoporous titanium oxide (TiO_x), both deposited at low temperature,[5,52,53] were used as electron contacts. In the first generation of solar cells, we used methylammonium lead iodide ($MAPbI_3$) as an ABX_3 perovskite absorber (Figure 1a). Later, in the second generation of solar cells, a mixed-cation mixed-halide absorber containing formamidinium (FA) and cesium (Cs) on the *A* site and iodine (I) and bromine (Br) on the *X* site was used (Figure 1b). The optical band gap is around 1.7 eV, and thus more suitable for tandem solar cells. Prior to perovskite deposition, a blend of phenyl-C_{61}-butyric acid methyl ester and polymethyl methacrylate (PCBM:PMMA) was spin-coated as a passivation layer on the electron contact for enhanced voltage.[54] In the third generation of solar cells, a slightly different absorber composition was employed containing more Cs and less Br (Figure 1c). This adapted composition exhibits improved PL stability under constant illumination and slightly higher efficiencies while maintaining an optical band gap in the similar range compared to the second generation. In all generations, Spiro-OMeTAD was used as the hole transport layer. ITO was directly sputtered on Spiro-OMeTAD using a shadow mask defining four 6 mm × 6 mm large areas on each substrate. For the first two generations, a gold contact grid (finger width 100 μm, finger distance 1 mm) was evaporated on the ITO pads followed by a U-shaped busbar around the ITO pads. In the third generation, the grid was omitted, and only the busbar was used for contacting. Additionally, a magnesium fluoride (MgF_2) antireflection coating was evaporated. For current−voltage (*IV*) measurements, a shadow mask with an aperture area of 5 mm × 5 mm was used.

2.2. Optimization of ITO Sputter Process. ITO was direct current (DC) sputtered from a 507 cm^2 indium oxide/tin oxide target (In_2O_3/SnO_2 = 90:10 wt %). The starting point for the sputtering process variations was a process developed for depositions on sensitive hydrogenated amorphous silicon (a-Si:H) layers for silicon heterojunction solar cell contacts without unrecoverable degradation of the passivation quality. The sputter power was 200 W, and the chamber pressure was 0.3 Pa. The set temperature of the table

DOI: 10.1021/acsami.9b17241
ACS Appl. Mater. Interfaces 2019, 11, 45796−45804

can be adjusted and was kept at 100 °C. In contrast to the original process, the oxygen gas flow was set to 0 sccm for all experiments presented in this work to avoid any degradation from oxidation. The sputter time was chosen in a way that a layer thickness of ∼85 nm was achieved.

In the first experiment, the sputter power was decreased to reduce possible sputter damage of the Spiro-OMeTAD due to bombardment with high energetic ions.[50] The aim was that the bombardment would be less severe, and a softer process could be applied with a lower sputter power. In silicon heterojunction solar cells, degradation of the passivation quality of a-Si:H or polycrystalline silicon could be decreased by reducing the ITO sputter power.[55,56] The sputter time was adapted to keep the thickness constant. Interestingly, the performance of solar cells with ITO sputtered at lower power (40 W) is only slightly better than for the standard process (200 W). However, interpretation of the results is quite difficult due to a huge spread in the results, as it was unfortunately always the case for solar cells of the first generation with the $MAPbI_3$ absorber (Figure S1). Nevertheless, a slight improvement of ∼5−10% relative in efficiency can be seen considering the median value for sputter processes with 40 W. We also tested a shorter two-step process, where the first ∼30 nm are sputtered at 40 W before increasing the power to 200 W in the second step. The cells fabricated with the two-step process perform as well as those produced using only 40 W. Due to the savings in process time, the two-step process was chosen for further experiments.

In a second experiment, the set temperature of the table was varied. Jena et al. showed that perovskite solar cells containing Spiro-OMeTAD degraded after heating them over 60 °C and explained the performance drop with a chemical modification at the perovskite/Spiro-OMeTAD interface.[57] An obvious trend can also be seen in our results even though the first-generation cells (MAPbI3 absorber) were still used for this purpose, and thus the spread of the results is quite high (Figures 2 and S2). The temperature variation did not have any influence on the layer thickness, which was ∼85 nm for all tested temperatures. Solar cells processed at 50 °C have higher open-circuit voltages (V_{OC}) and fill factors (FF) compared to the values obtained from processes with higher temperatures (75 and 100 °C). No additional gain was achieved with an even lower temperature of 35 °C. Thus, 50 °C was chosen for further solar cell batches.

In the third experiment, the chamber pressure was increased. At a higher chamber pressure, more particles are available, decelerating the high energetic ions, which may result in a softer process.[58] Here, solar cells of the second generation (PCBM:PMMA passivation layer and $FA_{0.83}Cs_{0.17}Pb(I_{0.73}Br_{0.27})_3$ perovskite absorber) were used. Sputter power was again set to 200 W to make sure that the plasma ignites, which might not be the case for a combination of high chamber pressure and low sputter power. A reference group with the two-step process (40 W + 200 W) at a standard pressure of 0.3 Pa was also processed. Due to a lower spread in the results for the second-generation solar cells ($FA_{0.83}Cs_{0.17}Pb(I_{0.73}Br_{0.27})_3$ absorber), a more distinct difference between these references and the cells sputtered at 200 W can be seen (Figure S3) compared to the first batch with first-generation solar cells with the $MAPbI_3$ absorber (Figure S1). By increasing the chamber pressure (0.3, 0.7, 1.3, 1.3, and 2.7 Pa), no improvement in performance can be observed (Figure S3). In contrast, mean efficiency values are even lower for

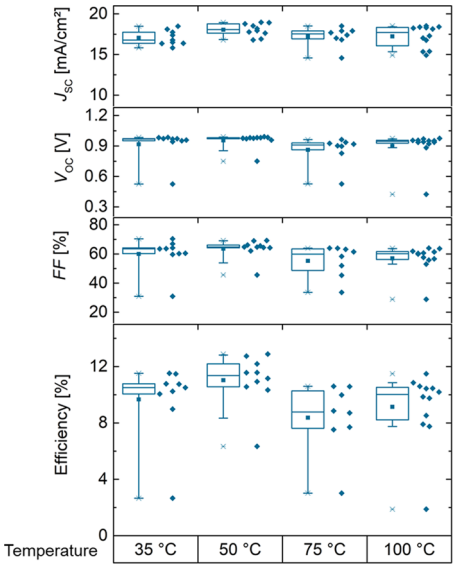

Figure 2. Performance of semi-transparent perovskite solar cells (glass/FTO/compact TiO_x/mesoporous TiO_x/ $MAPbI_3$/Spiro-OMeTAD/ITO/Au grid, first generation, see Figure 1a) depending on the temperature during ITO sputtering. 50% of the data points are within the boxes, 80% of the points within the whiskers. The point and horizontal line represent mean and median values, respectively. The two-step process (first 40 W, then 200 W) was used, the chamber pressure was at 0.3 Pa. Here, only results from reverse scan direction measured from the glass side are presented. All data, including both scan and illumination directions, can be found in Figure S2. The best performance was achieved at 50 °C.

higher pressures and the spread increased. It has to be noted that the thickness was not well controlled in this experiment and increased from 81 nm for 0.3 Pa to 89, 115, and 143 nm for 0.7, 1.3, and 2.7 Pa, respectively. However, at least for a thickness of ∼100 nm, this should not have a negative but rather a positive effect on cell performance, as will be discussed in the following section. A possible reason for the decreasing performance may be poor electronic bulk properties of the ITO for high chamber pressures (low mobility, high sheet resistance).[55] Thus, a chamber pressure of 0.3 Pa was maintained.

For ITO layers processed with the described optimized process mobility, resistivity, and charge carrier density are 42 $cm^2\ V^{-1}\ s^{-1}$, $4.5 \times 10^{-4}\ \Omega$ cm, and $3.4 \times 10^{20}\ cm^{-3}$, respectively, determined from Hall measurements.

2.3. Optical Improvements of Semi-Transparent Perovskite Solar Cells. With this optimized ITO process (first 40 W, then 200 W; 50 °C; 0.3 Pa), a thickness variation was executed using the second-generation perovskite solar cell architecture ($FA_{0.83}Cs_{0.17}Pb(I_{0.73}Br_{0.27})_3$ absorber and PCBM:PMMA passivation layer). For the first group of cells, only the 40 W step was applied, resulting in a 33 nm thick ITO layer. For the other groups, the two-step process was used with different times for the second 200 W step yielding in a total ITO film thickness of 57, 81, and 105 nm. Looking at the solar cell performance, similar efficiencies were achieved for all thicknesses, except for some outliers (Figure 3).

For all groups, efficiency is about 4% absolute higher when measuring from the glass side compared to results measured from the ITO side due to a huge difference in short-circuit current density (J_{SC}). This can also be observed in the aforementioned results (Figures S1−S3). There are three

DOI: 10.1021/acsami.9b17241
ACS Appl. Mater. Interfaces 2019, 11, 45796−45804

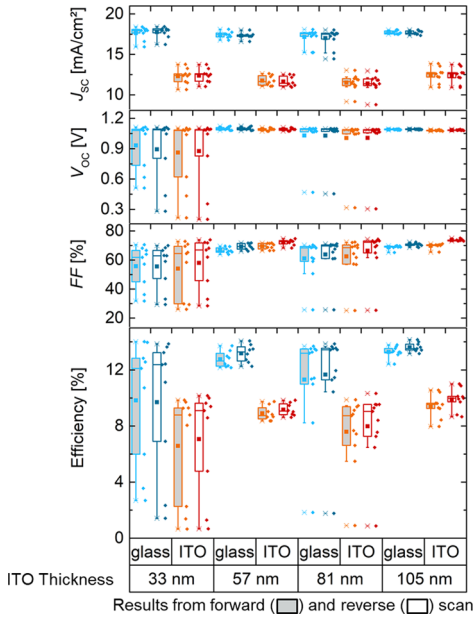

Figure 3. Performance of semi-transparent perovskite solar cells (glass/FTO/compact TiO_x/mesoporous TiO_x/PCBM:PMMA/$FA_{0.83}Cs_{0.17}Pb(I_{0.73}Br_{0.27})_3$/Spiro-OMeTAD/ITO/Au grid, second generation, see Figure 1b) illuminated from both sides depending on the ITO thickness (ITO process parameters: temperature: 50 °C; power: 40 W for the first ∼30 nm, then 200 W; pressure: 0.3 Pa). 50% of the data points are within the boxes, 80% of the points within the whiskers. The point and horizontal line represent mean and median values, respectively. Similar efficiencies are achieved for all thicknesses with the best devices for a 105 nm thick ITO layer. High reflection, parasitic absorption, and shading due to the grid fingers lead to a lower J_{SC} when illuminating the solar cells from the ITO side than from the glass side.

reasons for the large optical losses when light is coming from the ITO side. First, high parasitic absorption occurs in the Spiro-OMeTAD. Tucher et al. calculated the corresponding losses to be 1.1 mA cm^{-2} in a 50 nm thick Spiro-OMeTAD layer.[59] In our devices, the Spiro-OMeTAD is over 200 nm thick, which would result in even higher losses due to parasitic absorption. Second, the grid fingers shade ∼10% of the active cell area, reducing the amount of light entering the solar cell compared to the glass side. Third, the reflectance is significantly higher when illuminating from the ITO side over the whole wavelength range relevant for the perovskite solar cell (Figure 4). The reflection losses weighted by the Air Mass 1.5 global (AM 1.5 g) spectrum correspond to 1.3 and 3.4 mA cm^{-2} when measuring from the glass and ITO side, respectively. The higher loss from the ITO side is due to an inappropriate order of refractive indices. The light first passes through the ITO ($n \sim 2.0$ at 600 nm, determined from spectral ellipsometry measurement, Figure S4), then Spiro-OMeTAD ($n \sim 1.65$ at 600 nm[60]) before entering the perovskite ($n \sim 2.4$ at 600 nm[61]).

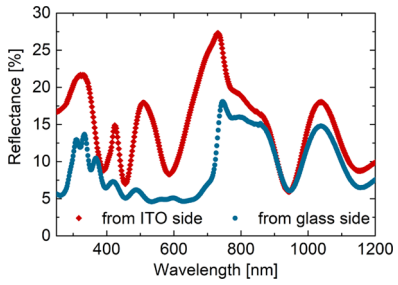

Figure 4. Reflectance measured from both sides of an optical sample with the same structure as the solar cells (105 nm ITO), except for the gold contacts. A significantly larger amount of light is reflected when illuminating the cells from the ITO side.

Measured from the glass side, no difference in J_{SC} can be seen in dependence on the ITO layer thickness. This is not surprising, as in this case, the ITO is just the rear contact. From the ITO side, a little enhanced current can be observed for the thinnest (33 nm) and thickest (105 nm) ITO layer compared to the thicknesses in between (57 and 81 nm) which will be discussed later. Looking carefully at the V_{OC}, one can see a slight decrease of the voltage with increasing ITO thickness from 57 to 105 nm. The same trend was observed by Jaysankar et al. and explained with increasing sputter damage with a longer sputter time.[51] However, for the investigated thicknesses presented in Figure 3, the difference is very small and the highest efficiency value was even reached with a 105 nm thick ITO. With thicker ITO layers, the sheet resistance R_{Sheet} is lower. In Hall measurements, R_{Sheet} has been determined to be 152, 82, 56, and 44 Ω sq^{-1} for the ITO thicknesses of 33, 57, 81, and 105 nm, respectively.

To enhance the current from the ITO side, a MgF_2 antireflection coating was applied to reduce front side reflection. Therefore, the transmittance weighted by the AM 1.5 g spectrum was calculated in dependence of the ITO and MgF_2 layer thicknesses using the transfer matrix formalism.[62] In this simulation, the perovskite was used as a substrate. For the perovskite, Spiro-OMeTAD and MgF_2 optical constants from the literature were used.[60,61,63] The refractive index n and extinction coefficient k of ITO have been determined by spectral ellipsometry (Figure S4). For the weighting, a spectral range from 350 to 730 nm relevant for the mixed-cation mixed-halide perovskites was used in this work. Simulation results are shown in Figure 5. Without MgF_2, a minimum of weighted transmittance into the perovskite (73.7%) can be seen for an ITO thickness of 69 nm increasing for thinner and thicker layers. The maximal difference of the weighted transmittance

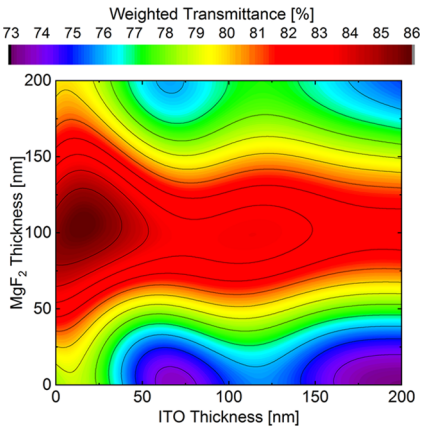

Figure 5. Transmittance into the perovskite weighted by the AM 1.5 g spectrum in the wavelength range relevant for a perovskite solar cell (350−730 nm) in dependence of the ITO and MgF_2 layer thicknesses calculated using the transfer matrix formalism. For all ITO thicknesses, transmittance into the perovskite can be significantly enhanced using a ∼100 nm thick antireflection coating.

DOI: 10.1021/acsami.9b17241
ACS Appl. Mater. Interfaces 2019, 11, 45796−45804

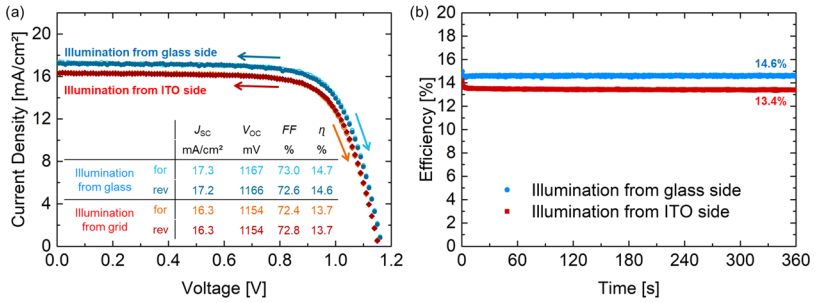

Figure 6. (a) *IV* curves and (b) stabilized measurements of the best performing cells (glass/FTO/compact TiO_x/mesoporous TiO_x/PCBM:PMMA/$FA_{0.75}Cs_{0.25}Pb(I_{0.80}Br_{0.20})_3$/Spiro-OMeTAD/ITO/$MgF_2$, third generation, see Figure 1c) from glass and ITO side. Due to the omission of the contact grid and antireflection coating, the current from the ITO side is enhanced and the difference between efficiency obtained from illumination from the glass and the ITO side could be reduced.

for the investigated ITO thicknesses is rather small (74.0% for an 81 nm and 76.8% for a 33 nm thick ITO layer, respectively) and corresponds to 0.7 mA cm^{-2}. The trend is in agreement with the J_{SC} values obtained from the measurement from the ITO side shown in Figure 3. Using an 80−120 nm thick MgF_2 antireflection coating significantly improves the weighted transmittance for all ITO thicknesses.

For the next experiment, third-generation perovskite cells with a $FA_{0.75}Cs_{0.25}Pb(I_{0.80}Br_{0.20})_3$ absorber and a MgF_2 antireflection coating were used. Although the maximum transmittance of over 85% occurs for very thin ITO layers (<30 nm), a transmittance of over 83% can be achieved also with thicker layers over 100 nm with a distinctly lower R_{Sheet}. Here, the thicker layer was retained as it allows to omit the contact grid for reduced shading losses. Both measures, applying an antireflection coating and omitting the grid, show a gain in the current (Figure S5). The difference in efficiency in the results obtained from measurements from the glass or ITO side is decreased to <2% absolute. No decrease in the fill factor (FF) can be seen for the solar cells without a grid, meaning that R_{Sheet} of the ITO is low enough that no significant contribution to the series resistance R_S of the perovskite solar cell is coming from the ITO. The best semi-transparent solar cells achieve 14.6 and 13.4% stabilized efficiencies from the glass and ITO side, respectively (Figure 6). The highest current from the ITO side is 16.3 mA cm^{-2}.

2.4. Four-Terminal Tandem Performance Estimation. The transmittance of the semi-transparent perovskite solar cells could be significantly enhanced due to the omission of the contact grid and the application of an antireflection coating compared to second-generation solar cells ($FA_{0.83}Cs_{0.17}Pb(I_{0.73}Br_{0.27})_3$ absorber, contact grid, no MgF_2 antireflection coating) processed before ITO layer thickness optimization. This holds true for the whole wavelength range relevant to a silicon bottom solar cell in a tandem device (Figure 7). To reduce reflection losses at the glass side, an additional MgF_2 antireflection coating was applied on the glass of the best solar cell shown in Figure 6. Afterward, the stabilized efficiency was 14.8%.

The transmittance curves shown in Figure 7 can be used to estimate the efficiency of a four-terminal perovskite silicon tandem solar cell. For this purpose, a high-efficiency silicon solar (24.9%) cell was measured under different irradiances and its efficiency in dependence of the J_{SC} was determined (Figure S 6). The J_{SC} of the silicon solar cell in a four-terminal configuration can be obtained by integration over the external quantum efficiency multiplied by the transmittance of the

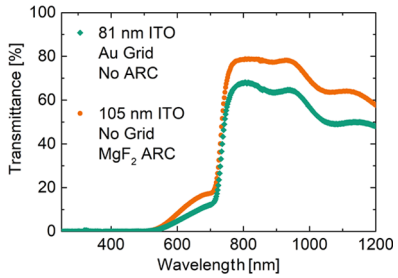

Figure 7. Transmittance of a second-generation perovskite solar cell ($FA_{0.83}Cs_{0.17}Pb(I_{0.73}Br_{0.27})_3$ absorber, contact grid, no MgF_2 antireflection coating) before ITO layer thickness optimization, and a third-generation solar cell ($FA_{0.75}Cs_{0.25}Pb(I_{0.80}Br_{0.20})_3$ absorber, no contact grid, MgF_2 antireflection coating) with an additional MgF_2 layer on the glass. Due to antireflection coatings and omission of the grid, transmittance could significantly be enhanced.

perovskite solar cell and the AM 1.5 g spectrum. Using the transmittance of the perovskite solar cell of the second generation ($FA_{0.83}Cs_{0.17}Pb(I_{0.73}Br_{0.27})_3$ absorber, contact grid, no MgF_2 antireflection coating), the silicon bottom solar cell would generate a J_{SC} of 13.6 mA cm^{-2}; for the optically better solar cell of the third generation ($FA_{0.75}Cs_{0.25}Pb(I_{0.80}Br_{0.20})_3$ absorber, no contact grid, MgF_2 antireflection coating), this value can be enhanced to 16.8 mA cm^{-2} (Figure S7). Due to the different areas, the silicon solar cell was not measured directly with the perovskite solar cell on top. The filtered efficiencies of the bottom solar cell are 7.5 and 9.4% resulting in four-terminal efficiencies of 21.8 and 24.2%, respectively (Tables 1 and 2). In a four-terminal configuration, the perovskite solar cell can be illuminated from the better side, i.e., from the glass side in this case. However, a highly efficient silicon solar cell outperforms the tandem device showing that further improvement is needed.

3. DISCUSSION

Our results are comparable to the semi-transparent perovskite solar cells without the buffer layer between Spiro-OMeTAD and ITO presented by Jaysankar et al., who achieved efficiencies of up to 14.4% on 0.13 cm^2 large solar cells.[51] In their publication, they present a higher J_{SC} but a lower V_{OC}, which can be explained with the perovskite absorber. They used $MAPbI_3$ with a lower band gap than the mixed-cation mixed-halide absorber used in our record device.

Adding an antireflection coating and omitting the contact grid could significantly improve the current when measuring from the ITO side. It has to be noted that for future cell areas

DOI: 10.1021/acsami.9b17241
ACS Appl. Mater. Interfaces 2019, 11, 45796−45804

Table 1. Comparison of Four-Terminal Device Performance Using Different Perovskite Top Solar Cells

	tandem 1	tandem 2
generation of perovskite solar cells	2	3
perovskite absorber	$FA_{0.83}Cs_{0.17}Pb(I_{0.73}Br_{0.27})_3$	$FA_{0.75}Cs_{0.25}Pb(I_{0.80}Br_{0.20})_3$
contact grid fingers	yes	no
ITO thickness	80 nm	105 nm
MgF_2 antireflection coating	no	on both sides
perovskite solar cell efficiency	14.3%	14.8%
silicon solar cell efficiency (filtered)	7.5%	9.4%
four-terminal tandem solar cell efficiency	21.8%	24.2%

Table 2. Photovoltaic Parameters of the Solar Cells Used for the Four-Terminal Performance Estimation

	J_{SC} (mA cm^{-2})	V_{OC} (V)	*FF* (%)	efficiency (%)
silicon solar cell	43.2	0.71	81	24.9
	Tandem 1			
perovskite solar cell forward scan	18.3	1.08	72	14.3
perovskite solar cell reverse scan	18.2	1.09	71	14.1
perovskite solar cell stabilized				14.3
silicon solar cell filtered	13.6	0.68	80	07.5
four-terminal tandem device				21.8
	Tandem 2			
perovskite solar cell forward scan	17.4	1.17	74	15.0
perovskite solar cell reverse scan	17.3	1.17	74	14.8
perovskite solar cell stabilized				14.8
silicon solar cell filtered	16.8	0.69	81	09.4
four-terminal tandem device				24.2

larger than 0.25 cm^2 grid fingers might be needed again. However, their distance can be adapted according to the good conductivity of our ITO. For this optimization, further experiments or simulations would be required.

For further improvement, Spiro-OMeTAD needs to be replaced by a material with higher refractive index lowering reflection losses and lower extinction coefficient reducing parasitic absorption. The candidate might be copper thiocyanate (CuSCN), which was already used in perovskite solar cells with over 20% efficiency and whose optical constants are more suitable than in the case of Spiro-OMeTAD.[64,65]

In the literature, semi-transparent perovskite solar cells with similar cell architectures and ∼1.7 eV optical band gap absorbers reach over 15% efficiency. Our devices have an FF in a similar range and even a slightly higher V_{OC}.[9,31] However, our solar cells suffer from a lower current, also when measuring from the optically better glass side. Looking at the transmittance of the optically optimized solar cells (Figure 7), a part of the light is transmitted through the perovskite solar cell above the band gap. This loss corresponds to ∼1.6 mA cm^{-2} and might be reduced by an increase of the perovskite absorber layer thickness.

4. CONCLUSIONS

In this paper, we presented semi-transparent perovskite solar cells in the n−i−p architecture with an ITO contact layer directly sputtered on the hole transporting material. No additional buffer layer is needed between Spiro-OMeTAD and ITO. Sputter parameters were systematically varied. A slight improvement could be seen for starting the process at a low sputter power before increasing to a higher power, whereas no improvement was observed for enhanced chamber pressures. Temperature optimization was crucial. The best results were achieved at 50 °C. At higher temperatures, V_{OC} and FF decreased. In a thickness variation, the best results were achieved for a 105 nm thick ITO layer. The sheet resistance of 44 Ω sq^{-1} allowed for omitting the contact grid fingers without FF loss, and thus, enhancing the current when illuminating from the ITO side. With an additional MgF_2 antireflection coating, efficiencies of up to 13.4% could be achieved. From the optically favored glass side, 14.8% efficiency was achieved when applying an antireflection coating also on the glass. Combining this cell with a silicon bottom solar cell in a four-terminal configuration, an efficiency of 24.2% was estimated.

5. EXPERIMENTAL DETAILS

5.1. Device Fabrication. Semi-transparent perovskite solar cells were fabricated on commercial fluorine-doped tin oxide (FTO)-coated glass substrates (AMG, 7 Ω sq^{-1}). The substrates were cleaned in an ultrasonic bath with a detergent and ethanol. Subsequently, a 20 nm thick compact TiO_2 electron transport layer was evaporated in a Pfeiffer PLS 570 evaporation tool with a voltage electron gun (Telemark model 267). Afterward, 150 mL of a solution containing a commercial TiO_2 paste (Dyesol 18NR-T) diluted in terpineol (65% α, 10% β, 20% γ, Sigma-Aldrich) and ethanol (99.5%, Carl Roth) in a mass ratio of 1:4:2 were spin-coated at 2500 rpm for 10 s and 7000 rpm for 40 s. The samples were then dried at 120 °C for 10 min. The whole procedure was repeated before the samples were exposed to UV irradiation in a UV/Ozone Cleaner Plus from Bioforce Nanosciences for 200 min. More detailed information about the low-temperature process for the electron contact can be found in our previous work.[52,53] Hereafter, samples were transferred to a nitrogen-filled glovebox and annealed at 120 °C for 15 min. As proposed by Peng et al., we used a PCBM:PMMA passivation layer on top of the electron contact. Therefore, 70 mL of a solution containing 1 mg/mL PMMA (MW ∼ 120 000, Sigma-Aldrich) and 3 mg/mL PCBM (Solenne) in chlorobenzene (Carl Roth) was spin-coated at 5000 rpm for 30 s.[54]

For the first-generation solar cells, the perovskite ($MAPbI_3$) was prepared as described in our previous work.[52] In the case of the second generation, a mixed cation mixed halide perovskite with the composition of $FA_{0.83}Cs_{0.17}Pb(I_{0.73}Br_{0.27})_3$ was used. A 1 M precursor solution of formamidinium iodide (FAI, Greatcell Solar), cesium iodide (CsI, 99 999%, Sigma-Aldrich), lead bromide ($PbBr_2$, 99 999%, Sigma-Aldrich), and lead iodide (PbI_2, 9999%, TCI) diluted in dimethyl sulfoxide (DMSO, ≥99.9%, Sigma-Aldrich) and dimethylformamide(DMF, 99,8%, Sigma-Aldrich) in a volume ratio of 1:4 was prepared and stirred overnight at 60 °C. Then, 100 μL of this solution was spin-coated at 1000 rpm for 10 s and 5000 rpm for 20 s. Five seconds prior to the end of the process, 200 μL of toluene (≥99.5%, Carl Roth) was added as an antisolvent. Subsequently, the samples were kept on a hot plate at ∼95 °C for 1 h. For the third generation, a perovskite composition ($FA_{0.75}Cs_{0.25}Pb(I_{0.80}Br_{0.20})_3$) proposed by Bush et al. was used.[7] Again, a 1 M precursor solution containing FAI, CsI, $PbBr_2$, and PbI_2 in DMSO and DMF (volume ratio 1:4) was prepared and stirred overnight at 60 °C. Then, 150 μL

DOI: 10.1021/acsami.9b17241
ACS Appl. Mater. Interfaces 2019, 11, 45796−45804

of this solution was spin-coated with the same parameters as in the case of the second generation ($FA_{0.83}Cs_{0.17}Pb(I_{0.73}Br_{0.27})_3$ absorber).

For the hole transport layer, we used a mixture of 56 mg Spiro-OMeTAD (Solarpur) in 650 μL chlorobenzene with 14 μL of a stock solution containing 50 mg bis(trifluoromethane)sulfonamide lithium salt (Sigma-Aldrich) in 80 μL acetonitrile (Merck) and 20 μL 4-*tert*-butylpyridine (96%, Sigma-Aldrich). This Spiro-OMeTAD precursor solution was kept in the nitrogen-filled glovebox for 3 h before usage. Then, 65 μL per sample was distributed over the substrate, kept for 30 s, and then spin-coated at 3000 rpm for 30 s.

ITO was deposited by DC sputtering (In_2O_3/SnO_2 = 90:10 wt %) in an Oxford Instruments Clustertool. A shadow mask with four openings (each 6 mm × 6 mm) per substrate was used to define four individual cells on each substrate. ITO process parameters were successively varied as described in the main text. For the optimized process, a temperature of 50 °C and a chamber pressure of 0.3 Pa were used. Sputter power was first at 40 W and then at 200 W. The respective deposition rates are ∼0.09 and ∼0.4 nm s^{-1}. A summary of all process parameters used in this work can be found in Table S1.

Solar cells of the first ($MAPbI_3$ absorber) and second ($FA_{0.83}Cs_{0.17}Pb(I_{0.73}Br_{0.27})_3$ absorber) generation were finished by thermally evaporating 150−200 nm thick gold fingers on the ITO and electrodes around the ITO pads. For the third generation ($FA_{0.75}Cs_{0.25}Pb(I_{0.80}Br_{0.20})_3$ absorber), only the surrounding electrodes were evaporated and, additionally, a 90 nm thick MgF_2 antireflection coating was thermally evaporated. Gold and MgF_2 evaporation were carried out in a Leybold Univex 350G evaporation tool at a high vacuum (<10^{-5} mbar).

5.2. Characterization. *IV* curves were measured using a sun simulator equipped with a Xenon short-arc lamp and a Keithley 2651A source meter. The system was calibrated to 1 sun illumination under the AM 1.5 g spectrum by adjusting the current of a silicon reference solar cell. All perovskite solar cells were measured first in forward (from −0.1 to 1.2 V) and then in reverse (from 1.2 to −0.1 V) scan direction. Scan speed and step size were 25 mV s^{-1} and 10 mV, respectively. To determine a stabilized efficiency, a fixed voltage (the mean voltage of the voltages at maximum power point obtained from forward and reverse scan) was applied, and the current was measured over time. A black shadow mask was used to define an active cell area of 0.25 cm^2. It has to be noted that the efficiency of the solar cells increased with several measurements until a certain performance level was reached, and always the result of the best measurement is represented.

Reflectance and transmittance were measured using a UV−vis spectrophotometer (Lambda 950 from PerkinElmer). The step size was 2 nm.

The refractive index n and the extinction coefficient k of ITO were determined by spectral ellipsometry using a J.A. Woollam M-2000 ellipsometer. An oscillator model containing a Gaussian and a Lorentz oscillator was fitted to the measured data. ITO layer thickness was also determined from this model or from fitting a Cauchy model in the nonabsorbing spectral range. Ellipsometry measurements were carried out on silicon samples included in each ITO process.

The electrical bulk properties of ITO films deposited on glass were determined by Hall Effect measurements in the van der Pauw geometry.

■ ASSOCIATED CONTENT

Supporting Information

The Supporting Information is available free of charge at https://pubs.acs.org/doi/10.1021/acsami.9b17241.

Performance of semi-transparent perovskite solar cells depending on sputter power, temperature, and chamber pressure; optical constants of ITO; influence of a MgF_2 antireflection coating and the omission of the contact grid on the performance of semi-transparent perovskite solar cells; dependence of a silicon solar cell efficiency on the J_{SC}; filtered EQE of the silicon solar cell for four-terminal performance estimation, and overview on ITO sputter parameters for all experiments (PDF)

■ AUTHOR INFORMATION

Corresponding Author

*E-mail: alexander.bett@ise.fraunhofer.de

ORCID

Alexander J. Bett: 0000-0003-0312-6701

Ludmila Cojocaru: 0000-0002-3618-4142

Patricia S. C. Schulze: 0000-0002-1924-6153

Author Contributions

This manuscript was written through contributions of all authors. All authors have given approval to the final version of the manuscript.

Notes

The authors declare no competing financial interest.

■ ACKNOWLEDGMENTS

This work was partially funded by the German Federal Ministry for Economic Affairs and Energy under contract number 0324037A (PersiST) and from the European Union's Horizon 2020 research and innovation program under grant agreement no. 641023 (Nano-Tandem). A.J.B. gratefully acknowledges scholarship support from the Deutsche Bundesstiftung Umwelt (DBU). The authors would like to thank K. Fischer, N. Garder, F. Gerspacher, D. Kurt, K. Saddedine, H. Steidl, K. Wienands, L. Zafoschnig, and K. Zimmermann for support in processing and measurements and O. Höhn for providing the transfer matrix formalism implementation script for the optical calculations.

■ REFERENCES

(1) Wolf, S. d.; Holovsky, J.; Moon, S.-J.; Löper, P.; Niesen, B.; Ledinsky, M.; Haug, F.-J.; Yum, J.-H.; Ballif, C. Organometallic Halide Perovskites: Sharp Optical Absorption Edge and Its Relation to Photovoltaic Performance. *J. Phys. Chem. Lett.* **2014**, *5*, 1035−1039.

(2) Ke, W.; Fang, G.; Liu, Q.; Xiong, L.; Qin, P.; Tao, H.; Wang, J.; Lei, H.; Li, B.; Wan, J.; Yang, G.; Yan, Y. Low-Temperature Solution-Processed Tin Oxide as an Alternative Electron Transporting Layer for Efficient Perovskite Solar Cells. *J. Am. Chem. Soc.* **2015**, *137*, 6730−6733.

(3) Habisreutinger, S. N.; Leijtens, T.; Eperon, G. E.; Stranks, S. D.; Nicholas, R. J.; Snaith, H. J. Carbon Nanotube/Polymer Composites as a Highly Stable Hole Collection Layer in Perovskite Solar Cells. *Nano Lett.* **2014**, *14*, 5561−5568.

(4) Ke, W.; Zhao, D.; Grice, C. R.; Cimaroli, A. J.; Fang, G.; Yan, Y. Efficient Fully-Vacuum-Processed Perovskite Solar Cells Using Copper Phthalocyanine as Hole Selective Layers. *J. Mater. Chem. A* **2015**, *3*, 23888−23894.

(5) Cojocaru, L.; Wienands, K.; Kim, T. W.; Uchida, S.; Bett, A. J.; Rafizadeh, S.; Goldschmidt, J. C.; Glunz, S. W. Detailed Investigation of Evaporated Perovskite Absorbers with High Crystal Quality on Different Substrates. *ACS Appl. Mater. Interfaces* **2018**, *10*, 26293−26302.

(6) NREL. Best Research-Cell Efficiencies. https://www.nrel.gov/pv/cell-efficiency.html (accessed November 4, 2019).

(7) Bush, K. A.; Frohna, K.; Prasanna, R.; Beal, R. E.; Leijtens, T.; Swifter, S. A.; McGehee, M. D. Compositional Engineering for Efficient Wide Band Gap Perovskites with Improved Stability to Photoinduced Phase Segregation. *ACS Energy Lett.* **2018**, *3*, 428−435.

(8) Jesper Jacobsson, T.; Correa-Baena, J.-P.; Pazoki, M.; Saliba, M.; Schenk, K.; Grätzel, M.; Hagfeldt, A. Exploration of the Compositional Space for Mixed Lead Halogen Perovskites for High Efficiency Solar Cells. *Energy Environ. Sci.* **2016**, *9*, 1706−1724.

DOI: 10.1021/acsami.9b17241
ACS Appl. Mater. Interfaces 2019, 11, 45796−45804

(9) McMeekin, D. P.; Sadoughi, G.; Rehman, W.; Eperon, G. E.; Saliba, M.; Horantner, M. T.; Haghighirad, A.; Sakai, N.; Korte, L.; Rech, B.; Johnston, M. B.; Herz, L. M.; Snaith, H. J. A Mixed-Cation Lead Mixed-Halide Perovskite Absorber for Tandem Solar Cells. *Science* **2016**, *351*, 151−155.
(10) Yoshikawa, K.; Kawasaki, H.; Yoshida, W.; Irie, T.; Konishi, K.; Nakano, K.; Uto, T.; Adachi, D.; Kanematsu, M.; Uzu, H.; Yamamoto, K. Silicon Heterojunction Solar Cell with Interdigitated Back Contacts for a Photoconversion Efficiency over 26%. *Nat. Energy* **2017**, *2*, No. 17032.
(11) Richter, A.; Hermle, M.; Glunz, S. W. Reassessment of the Limiting Efficiency for Crystalline Silicon Solar Cells. *IEEE J. Photovoltaics* **2013**, *3*, 1184−1191.
(12) Yamaguchi, M.; Lee, K.-H.; Araki, K.; Kojima, N. A Review of Recent Progress in Heterogeneous Silicon Tandem Solar Cells. *J. Phys. D: Appl. Phys.* **2018**, *51*, No. 133002.
(13) Ramírez Quiroz, C. O.; Shen, Y.; Salvador, M.; Forberich, K.; Schrenker, N.; Spyropoulos, G. D.; Heumüller, T.; Wilkinson, B.; Kirchartz, T.; Spiecker, E.; Verlinden, P. J.; Zhang, X.; Green, M. A.; Ho-Baillie, A.; Brabec, C. J. Balancing Electrical and Optical Losses for Efficient 4-Terminal Si−Perovskite Solar Cells with Solution Processed Percolation Electrodes. *J. Mater. Chem. A* **2018**, *6*, 3583−3592.
(14) Sahli, F.; Werner, J.; Kamino, B. A.; Bräuninger, M.; Monnard, R.; Paviet-Salomon, B.; Barraud, L.; Ding, L.; Diaz Leon, J. J.; Sacchetto, D.; Cattaneo, G.; Despeisse, M.; Boccard, M.; Nicolay, S.; Jeangros, Q.; Niesen, B.; Ballif, C. Fully Textured Monolithic Perovskite/Silicon Tandem Solar Cells with 25.2% Power Conversion Efficiency. *Nat. Mater.* **2018**, *17*, 820.
(15) Bush, K. A.; Manzoor, S.; Frohna, K.; Yu, Z. J.; Raiford, J. A.; Palmstrom, A. F.; Wang, H.-P.; Prasanna, R.; Bent, S. F.; Holman, Z. C.; McGehee, M. D. Minimizing Current and Voltage Losses to Reach 25% Efficient Monolithic Two-Terminal Perovskite−Silicon Tandem Solar Cells. *ACS Energy Lett.* **2018**, *3*, 2173−2180.
(16) Jošt, M.; Köhnen, E.; Morales-Vilches, A. B.; Lipovšek, B.; Jäger, K.; Macco, B.; Al-Ashouri, A.; Krč, J.; Korte, L.; Rech, B.; Schlatmann, R.; Topič, M.; Stannowski, B.; Albrecht, S. Textured Interfaces in Monolithic Perovskite/Silicon Tandem Solar Cells: Advanced Light Management for Improved Efficiency and Energy Yield. *Energy Environ. Sci.* **2018**, *2*, 3511−3523.
(17) Oxford PV. Oxford PV Perovskite Solar Cell Achieves 28% Efficiency: Perovskite Solar Technology Leader's Solar Cell Sets New World Record. https://www.oxfordpv.com/news/oxford-pv-perovskite-solar-cell-achieves-28-efficiency. (accessed Nov 13, 2019).
(18) Bailie, C. D.; Christoforo, M. G.; Mailoa, J. P.; Bowring, A. R.; Unger, E. L.; Nguyen, W. H.; Burschka, J.; Pellet, N.; Lee, J. Z.; Grätzel, M.; Noufi, R.; Buonassisi, T.; Salleo, A.; McGehee, M. D. Semi-Transparent Perovskite Solar Cells for Tandems with Silicon and CIGS. *Energy Environ. Sci.* **2015**, *8*, 956−963.
(19) Guo, F.; Azimi, H.; Hou, Y.; Przybilla, T.; Hu, M.; Bronnbauer, C.; Langner, S.; Spiecker, E.; Forberich, K.; Brabec, C. J. High-Performance Semitransparent Perovskite Solar Cells with Solution-Processed Silver Nanowires as Top Electrodes. *Nanoscale* **2015**, *7*, 1642−1649.
(20) Lang, F.; Gluba, M. A.; Albrecht, S.; Rappich, J.; Korte, L.; Rech, B.; Nickel, N. H. Perovskite Solar Cells with Large-Area CVD-Graphene for Tandem Solar Cells. *J. Phys. Chem. Lett.* **2015**, *6*, 2745−2750.
(21) You, P.; Liu, Z.; Tai, Q.; Liu, S.; Yan, F. Efficient Semitransparent Perovskite Solar Cells with Graphene Electrodes. *Adv. Mater.* **2015**, *27*, 3632−3638.
(22) Yang, Y. M.; Chen, Q.; Hsieh, Y.-T.; Song, T.-B.; Marco, N.; de Zhou, H.; Yang, Y. Multilayer Transparent Top Electrode for Solution Processed Perovskite/Cu(In,Ga)(Se,S)2 Four Terminal Tandem Solar Cells. *ACS Nano* **2015**, *9*, 7714−7721.
(23) Chen, B.; Bai, Y.; Yu, Z.; Li, T.; Zheng, X.; Dong, Q.; Shen, L.; Boccard, M.; Gruverman, A.; Holman, Z.; Huang, J. Efficient Semitransparent Perovskite Solar Cells for 23.0%-Efficiency Perovskite/Silicon Four-Terminal Tandem cells. *Adv. Energy Mater.* **2016**, *6*, No. 1601128.
(24) Kanda, H.; Uzum, A.; Nishino, H.; Umeyama, T.; Imahori, H.; Ishikawa, Y.; Uraoka, Y.; Ito, S. Interface Optoelectronics Engineering for Mechanically Stacked Tandem Solar Cells Based on Perovskite and Silicon. *ACS Appl. Mater. Interfaces* **2016**, *8*, 33553−33561.
(25) Ahn, J.; Hwang, H.; Jeong, S.; Moon, J. Metal-Nanowire-Electrode-Based Perovskite Solar Cells: Challenging Issues and New Opportunities. *Adv. Energy Mater.* **2017**, *7*, No. 1602751.
(26) Werner, J.; Niesen, B.; Ballif, C. Perovskite/Silicon Tandem Solar Cells: Marriage of Convenience or True Love Story? - An Overview. *Adv. Mater. Interfaces* **2018**, *5*, No. 1700731.
(27) Bush, K. A.; Bailie, C. D.; Chen, Y.; Bowring, A. R.; Wang, W.; Ma, W.; Leijtens, T.; Moghadam, F.; McGehee, M. D. Thermal and Environmental Stability of Semi-Transparent Perovskite Solar Cells for Tandems Enabled by a Solution-Processed Nanoparticle Buffer Layer and Sputtered ITO Electrode. *Adv. Mater.* **2016**, *28*, 3937−3943.
(28) Löper, P.; Moon, S.-J.; Martin de Nicolas, S.; Niesen, B.; Ledinsky, M.; Nicolay, S.; Bailat, J.; Yum, J.-H.; Wolf, S. d.; Ballif, C. Organic-Inorganic Halide Perovskite/Crystalline Silicon Four-Terminal Tandem Solar Cells. *Phys. Chem. Chem. Phys.* **2015**, *17*, 1619−1629.
(29) Fan, R.; Zhou, N.; Zhang, L.; Yang, R.; Meng, Y.; Li, L.; Guo, T.; Chen, Y.; Xu, Z.; Zheng, G.; Huang, Y.; Li, L.; Qin, L.; Qiu, X.; Chen, Q.; Zhou, H. Toward Full Solution Processed Perovskite/Si Monolithic Tandem Solar Device With PCE Exceeding 20%. *Sol. RRL* **2017**, *1*, No. 1700149.
(30) Jaysankar, M.; Filipič, M.; Zielinski, B.; Schmager, R.; Song, W.; Qiu, W.; Paetzold, U. W.; Aernouts, T.; Debucquoy, M.; Gehlhaar, R.; Poortmans, J. Perovskite−Silicon Tandem Solar Modules with Optimised Light Harvesting. *Energy Environ. Sci.* **2018**, *11*, 1489−1498.
(31) Duong, T.; Wu, Y.; Shen, H.; Peng, J.; Fu, X.; Jacobs, D.; Wang, E.-C.; Kho, T. C.; Fong, K. C.; Stocks, M.; Franklin, E.; Blakers, A.; Zin, N.; McIntosh, K. R.; Li, W.; Cheng, Y.-B.; White, T. P.; Weber, K.; Catchpole, K. Rubidium Multication Perovskite with Optimized Bandgap for Perovskite-Silicon Tandem with over 26% Efficiency. *Adv. Energy Mater.* **2017**, *7*, No. 1700228.
(32) Albrecht, S.; Saliba, M.; Correa Baena, J. P.; Lang, F.; Kegelmann, L.; Mews, M.; Steier, L.; Abate, A.; Rappich, J.; Korte, L.; Schlatmann, R.; Mohammad, K. N.; Hagfeldt, A.; Grätzel, M.; Rech, B. Monolithic Perovskite/Silicon-Heterojunction Tandem Solar Cells Processed at Low Temperature. *Energy Environ. Sci.* **2016**, *9*, 81−88.
(33) Bush, K. A.; Palmstrom, A. F.; Yu, Z. J.; Boccard, M.; Cheacharoen, R.; Mailoa, J. P.; McMeekin, D. P.; Hoye, R. L. Z.; Bailie, C. D.; Leijtens, T.; Peters, I. M.; Minichetti, M. C.; Rolston, N.; Prasanna, R.; Sofia, S.; Harwood, D.; Ma, W.; Moghadam, F.; Snaith, H. J.; Buonassisi, T.; Holman, Z. C.; Bent, S. F.; McGehee, M. D. 23.6%-Efficient Monolithic Perovskite/Silicon Tandem Solar Cells with Improved Stability. *Nat. Energy* **2017**, *2*, No. 17009.
(34) Duong, T.; Lal, N.; Grant, D.; Jacobs, D.; Zheng, P.; Rahman, S.; Shen, H.; Stocks, M.; Blakers, A.; Weber, K.; White, T. P.; Catchpole, K. R. Semitransparent Perovskite Solar Cell With Sputtered Front and Rear Electrodes for a Four-Terminal Tandem. *IEEE J. Photovoltaics* **2016**, *6*, 679−687.
(35) Hou, F.; Yan, L.; Shi, B.; Chen, J.; Zhu, S.; Ren, Q.; An, S.; Zhou, Z.; Ren, H.; Wei, C.; Huang, Q.; Hou, G.; Chen, X.; Li, Y.; Ding, Y.; Wang, G.; Zhang, D.; Zhao, Y.; Zhang, X. Monolithic Perovskite/Silicon-Heterojunction Tandem Solar Cells with Open-Circuit Voltage of over 1.8 V. *ACS Appl. Energy Mater.* **2019**, *2*, 243−249.
(36) Zheng, J.; Mehrvarz, H.; Ma, F.-J.; Lau, C. F. J.; Green, M. A.; Huang, S.; Ho-Baillie, A. W. Y. 21.8% Efficient Monolithic Perovskite/Homo-Junction-Silicon Tandem Solar Cell on 16 cm. *ACS Energy Lett.* **2018**, *3*, 2299−2300.
(37) Werner, J.; Dubuis, G.; Walter, A.; Löper, P.; Moon, S.-J.; Nicolay, S.; Morales-Masis, M.; Wolf, S. d.; Niesen, B.; Ballif, C.

DOI: 10.1021/acsami.9b17241
ACS Appl. Mater. Interfaces 2019, 11, 45796−45804

Sputtered Rear Electrode with Broadband Transparency for Perovskite Solar Cells. *Sol. Energy Mater. Sol. Cells* **2015**, *141*, 407−413.
(38) Sahli, F.; Kamino, B. A.; Werner, J.; Bräuninger, M.; Paviet-Salomon, B.; Barraud, L.; Monnard, R.; Seif, J. P.; Tomasi, A.; Jeangros, Q.; Hessler-Wyser, A.; Wolf, S. d.; Despeisse, M.; Nicolay, S.; Niesen, B.; Ballif, C. Improved Optics in Monolithic Perovskite/Silicon Tandem Solar Cells with a Nanocrystalline Silicon Recombination Junction. *Adv. Energy Mater.* **2018**, *8*, No. 1701609.
(39) Wu, Y.; Di, Y.; Peng, J.; Duong, T.; Wan, Y.; Phang, P.; Shen, H.; Wu, N.; Barugkin, C.; Fu, X.; Surve, S.; Walter, D.; White, T.; Catchpole, K.; Weber, K.; et al. Monolithic Perovskite/Silicon-Homojunction Tandem Solar Cell with over 22% Efficiency. *Energy Environ. Sci.* **2017**, *10*, 2472−2479.
(40) Shen, H.; Duong, T.; Peng, J.; Jacobs, D.; Wu, N.; Gong, J.; Wu, Y.; Karuturi, S. K.; Fu, X.; Weber, K.; Xiao, X.; White, T. P.; Catchpole, K. Mechanically-Stacked Perovskite/CIGS Tandem solar Cells with Efficiency of 23.9% and Reduced Oxygen Sensitivity. *Energy Environ. Sci.* **2018**, *11*, 394−406.
(41) Dewi, H. A.; Wang, H.; Li, J.; Thway, M.; Sridharan, R.; Stangl, R.; Lin, F.; Aberle, A. G.; Mathews, N.; Bruno, A.; Mhaisalkar, S. G. Highly Efficient Semi-Transparent Perovskite Solar Cells for Four Terminal Perovskite-Silicon Tandems. *ACS Appl. Mater. Interfaces* **2019**, *11*, 34178−34187.
(42) Peng, J.; Duong, T.; Zhou, X.; Shen, H.; Wu, Y.; Mulmudi, H. K.; Wan, Y.; Zhong, D.; Li, J.; Tsuzuki, T.; Weber, K. J.; Catchpole, K. R.; White, T. P. Efficient Indium-Doped TiOx Electron Transport Layers for High-Performance Perovskite Solar Cells and Perovskite-Silicon Tandems. *Adv. Energy Mater.* **2016**, *7*, No. 1601768.
(43) Jeon, N. J.; Na, H.; Jung, E. H.; Yang, T.-Y.; Lee, Y. G.; Kim, G.; Shin, H.-W.; Il Seok, S.; Lee, J.; Seo, J. A Fluorene-Terminated Hole-Transporting Material for Highly Efficient and Stable Perovskite Solar Cells. *Nat. Energy* **2018**, *3*, 682−689.
(44) Bi, D.; Yi, C.; Luo, J.; Décoppet, J.-D.; Zhang, F.; Zakeeruddin, S. M.; Li, X.; Hagfeldt, A.; Grätzel, M. Polymer-Templated Nucleation and Crystal Growth of Perovskite Films for Solar Cells with Efficiency Greater than 21%. *Nat. Energy* **2016**, *1*, No. 16142.
(45) Saliba, M.; Matsui, T.; Domanski, K.; Seo, J.-Y.; Ummadisingu, A.; Zakeeruddin, S. M.; Correa-Baena, J.-P.; Tress, W. R.; Abate, A.; Hagfeldt, A.; Gratzel, M. Incorporation of Rubidium Cations into Perovskite Solar Cells Improves Photovoltaic Performance. *Science* **2016**, *354*, 206−209.
(46) Yang, D.; Yang, R.; Wang, K.; Wu, C.; Zhu, X.; Feng, J.; Ren, X.; Fang, G.; Priya, S.; Liu, S. F. High Efficiency Planar-Type Perovskite Solar Cells with Negligible Hysteresis Using EDTA-Complexed SnO2. *Nat. Commun.* **2018**, *9*, No. 3239.
(47) Yang, W. S.; Park, B.-W.; Jung, E. H.; Jeon, N. J.; Kim, Y. C.; Lee, D. U.; Shin, S. S.; Seo, J.; Kim, E. K.; Noh, J. H.; Seok, S. I. Iodide Management in Formamidinium-Lead-Halide-Based Perovskite Layers for Efficient Solar Cells. *Science* **2017**, *356*, 1376−1379.
(48) Werner, J.; Geissbuhler, J.; Dabirian, A.; Nicolay, S.; Morales-Masis, M.; Wolf, S. d.; Niesen, B.; Ballif, C. Parasitic Absorption Reduction in Metal Oxide-Based Transparent Electrodes: Application in Perovskite Solar Cells. *ACS Appl. Mater. Interfaces* **2016**, *8*, 17260−17267.
(49) Lal, N. N.; Dkhissi, Y.; Li, W.; Hou, Q.; Cheng, Y.-B.; Bach, U. Perovskite Tandem Solar Cells. *Adv. Energy Mater.* **2017**, *7*, No. 1602761.
(50) Fu, F.; Feurer, T.; Jager, T.; Avancini, E.; Bissig, B.; Yoon, S.; Buecheler, S.; Tiwari, A. N. Low-Temperature-Processed Efficient Semi-Transparent Planar Perovskite Solar Cells for Bifacial and Tandem Applications. *Nat. Commun.* **2015**, *6*, No. 8932.
(51) Jaysankar, M.; Qiu, W.; van Eerden, M.; Aernouts, T.; Gehlhaar, R.; Debucquoy, M.; Paetzold, U. W.; Poortmans, J. Four-Terminal Perovskite/Silicon Multijunction Solar Modules. *Adv. Energy Mater.* **2017**, *7*, No. 1602807.
(52) Schulze, P. S. C.; Bett, A. J.; Winkler, K.; Hinsch, A.; Lee, S.; Mastroianni, S.; Mundt, L. E.; Mundus, M.; Würfel, U.; Glunz, S. W.; Hermle, M.; Goldschmidt, J. C. Novel Low-Temperature Process for Perovskite Solar Cells with a Mesoporous TiO2 Scaffold. *ACS Appl. Mater. Interfaces* **2017**, *9*, 30567−30574.
(53) Bett, A. J.; Schulze, P. S. C.; Winkler, K.; Gasparetto, J.; Ndione, P. F.; Bivour, M.; Hinsch, A.; Kohlstädt, M.; Lee, S.; Mastroianni, S.; Mundt, L. E.; Mundus, M.; Reichel, C.; Richter, A.; Veit, C.; Wienands, K.; Würfel, U.; Veurman, W.; Glunz, S. W.; Hermle, M.; Goldschmidt, J. C. Low Temperature Perovskite Solar Cells with an Evaporated TiO2 Compact Layer for Perovskite Silicon Tandem Solar Cells. *Energy Procedia* **2017**, *124*, 567−576.
(54) Peng, J.; Wu, Y.; Ye, W.; Jacobs, D. A.; Shen, H.; Fu, X.; Wan, Y.; Duong, T.; Wu, N.; Barugkin, C.; Nguyen, H. T.; Zhong, D.; Li, J.; Lu, T.; Liu, Y.; Lockrey, M. N.; Weber, K. J.; Catchpole, K. R.; White, T. P. Interface Passivation Using Ultrathin Polymer−Fullerene Films for High-Efficiency Perovskite Solar Cells with Negligible Hysteresis. *Energy Eviron. Sci.* **2017**, *10*, 1792−1800.
(55) Tutsch, L.; Bivour, M.; Wolke, W.; Hermle, M.; Rentsch, J. In Influence of the Transparent Electrode Sputtering Process on the Interface Passivation Quality of Silicon Heterojunction Solar Cells, Proceedings of the 33rd European PV Solar Energy Conference and Exhibition, 2017.
(56) Tutsch, L.; Feldmann, F.; Polzin, J.; Luderer, C.; Bivour, M.; Moldovan, A.; Rentsch, J.; Hermle, M. Implementing Transparent Conducting Oxides by DC Sputtering on Ultrathin SiOx/Poly-Si Passivating Contacts. *Sol. Energy Mater. Sol. Cells* **2019**, *200*, No. 109960.
(57) Jena, A. K.; Numata, Y.; Ikegami, M.; Miyasaka, T. Role of Spiro-OMeTAD in Performance Deterioration of Perovskite Solar Cells at High Temperature and Reuse of the Perovskite Films to Avoid Pb-Waste. *J. Mater. Chem. A* **2018**, *6*, 2219−2230.
(58) Somekh, R. E. The Thermalization of Energetic Atoms During the Sputtering Process. *J. Vac. Sci. Technol. A* **1984**, *2*, 1285−1291.
(59) Tucher, N.; Höhn, O.; Bläsi, B.; Goldschmidt, J. C. Advanced Module Optics of Textured Perovskite Silicon Tandem Solar Cells. In *Photonics for Solar Energy*; Wehrspohn, R. B.; Sprafke, A. N., Eds.; SPIE, 2018; p 4.
(60) Filipič, M.; Löper, P.; Niesen, B.; de Wolf, S.; Krč, J.; Ballif, C.; Topič, M. CH3NH3PbI3 Perovskite/Silicon Tandem Solar Cells: Characterization Based Optical Simulations. *Opt. Express* **2015**, *23*, A263−A278.
(61) Werner, J.; Nogay, G.; Sahli, F.; Yang, T. C.-J.; Bräuninger, M.; Christmann, G.; Walter, A.; Kamino, B. A.; Fiala, P.; Löper, P.; Nicolay, S.; Jeangros, Q.; Niesen, B.; Ballif, C. Complex Refractive Indices of Cesium−Formamidinium-Based Mixed-Halide Perovskites with Optical Band Gaps from 1.5 to 1.8 eV. *ACS Energy Lett.* **2018**, *3*, 742−747.
(62) Macleod, H. A. *Thin Film Optical Filters*, 3rd ed.; Taylor & Francis, 2001.
(63) Bett, A. J. *Alternative Vorderseitenentspiegelungskonzepte von hocheffizienten, dünnen Siliciumsolarzellen*; Masterarbeit, Karlsruhe Institute of Technology: Karlsruhe, 2014.
(64) Arora, N.; Dar, M. I.; Hinderhofer, A.; Pellet, N.; Schreiber, F.; Zakeeruddin, S. M.; Grätzel, M. Perovskite Solar Cells with CuSCN Hole Extraction Layers Yield Stabilized Efficiencies Greater than 20%. *Science* **2017**, *358*, 768−771.
(65) Pattanasattayavong, P.; Ndjawa, G. O. N.; Zhao, K.; Chou, K. W.; Yaacobi-Gross, N.; O'Regan, B. C.; Amassian, A.; Anthopoulos, T. D. Electric Field-Induced Hole Transport in Copper(I) Thiocyanate (CuSCN) Thin-Films Processed from Solution at Room Temperature. *Chem. Commun.* **2013**, *49*, 4154−4156.

DOI: 10.1021/acsami.9b17241
ACS Appl. Mater. Interfaces 2019, 11, 45796−45804